Efficient 3D Multi-region Prostate MRI Segmentation Using Dual Optimization

Wu Qiu[1], Jing Yuan[1], Eranga Ukwatta[1,2], Yue Sun[1,2], Martin Rajchl[1,2], and Aaron Fenster[1,2]

[1] Robarts Research Institue
[2] Department of Biomedical Engineering,
Western University, London, Ontario, Canada
wqiu@imaging.robarts.ca

Abstract. Efficient and accurate extraction of the prostate, in particular its clinically meaningful sub-regions from 3D MR images, is of great interest in image-guided prostate interventions and diagnosis of prostate cancer. In this work, we propose a novel multi-region segmentation approach to simultaneously locating the boundaries of the prostate and its two major sub-regions: the central gland and the peripheral zone. The proposed method utilizes the prior knowledge of the spatial region consistency and employs a customized prostate appearance model to simultaneously segment multiple clinically meaningful regions. We solve the resulted challenging combinatorial optimization problem by means of convex relaxation, for which we introduce a novel spatially continuous flow-maximization model and demonstrate its duality to the investigated convex relaxed optimization problem with the region consistency constraint. Moreover, the proposed continuous max-flow model naturally leads to a new and efficient *continuous max-flow based* algorithm, which enjoys great advantages in numerics and can be readily implemented on GPUs. Experiments using 15 T2-weighted 3D prostate MR images, by inter- and intra-operator variability, demonstrate the promising performance of the proposed approach.

Keywords: 3D Prostate MRI, Zonal Segmentation, Convex Optimization.

1 Introduction

Prostate cancer is a major health problem in the western world, with one in six men affected during their lifetime [1]. In diagnosing prostate cancer, transrectal ultrasound (TRUS) guided biopsies have become the gold standard. However, the accuracy of the TRUS guided biopsy relies on and is limited by the fidelity. Magnetic resonance (MR) imaging is an attractive option for guiding and monitoring such interventions due to its superior visualization of not only the prostate, but also its substructure and the surrounding tissues [2,3]. The fusion of 3D TRUS and MRI provides an effective way to target biopsy needles in 3D TRUS images toward regions of the prostate containing MR identified suspicious lesions,

J.C. Gee et al. (Eds.): IPMI 2013, LNCS 7917, pp. 304–315, 2013.

which is regarded as an alternative to the more expensive and inefficient MRI-based prostate biopsy [4] and the less accurate conventional 2D TRUS-guieded prostate biopsy. The prostate consists of four zones: peripheral zone (PZ), central zone (CZ), transition zone (TZ), and fibromuscular stroma [5]. During guidance of the biopsy, the prostate is usually considered to have two visible zones on MRI: the *central gland* (CG) and the *peripheral zone* (PZ). The CG is assumed to be the outer contour of the prostate minus the PZ [6]. The reason for segmenting these regions is that up to 80% of prostate cancer are located within the PZ [7]. Thus, the ability to superimpose the 3D TRUS image used to guide the biopsy onto the pre-segmented regions of interest in MRI is highly desired in a fused 3D TRUS/MRI guided biopsy system. Computer aided diagnosis (CAD) techniques for prostate cancer can also benefit from the correct interpretation of the zonal anatomy of the prostate since the occurrence and appearance of cancer is dependent on its zonal location [8,9]. Furthermore, the ratio of CG volume to whole prostate gland (WG) can be used to monitor prostate hyperplasia [10].

Many studies have focused their efforts on whole prostate segmentation from in 3D MR images, especially in T2-weighted (T2w) 3D MR images, see [11] for a review of the existing literature. However, only a few studies focused on prostate zonal segmentation in 3D MRI. Allen *et al.* [12] proposed a method for automatic delineation of prostate boundaries and the CG. Unfortunately, the authors limited their segmentation to the middle region of the prostate (where T2w contrast permits accurate segmentation), and ignored the apex and base of the gland. Yin *et al.* [13] proposed an automated CG segmentation algorithm based on Layered Optimal Graph Image Segmentation of Multiple Objects and Surfaces (LOGISMOS). The test set indicated that their approach obtained a mean Dice Similarity Coefficient (DSC) of 80% for CG. The first paper about segmenting the prostate into the PZ and CG was proposed by Makni *et al.* [14]. The authors proposed a modified version of the evidential C-means algorithm to cluster voxels into their respective zones incorporating the spatial relation between voxels in 3D multispectral MR images including a T2w image, a diffusion weighted image (DWI), and a contrast enhanced MRI (CEMRI). The obtained mean DSCs were 87% for the central gland and 76% for the peripheral zone. More recently, Litjens *et al.* [15] proposed a pattern recognition method to classify the voxels using anatomical, intensity and texture features in multispectral MR images. Their method obtained a DSC of 89% for the central gland and 75% for the peripheral zone. However, in [14] and [15], the segmentation of prostate peripheral zone relies on the manual segmentation of the whole prostate gland. In [15], the authors additionally stated that they also developed an atlas-based method to segment the prostate zones at the same time without a manual whole prostate mask. Unfortunately, the method failed to give any favourable results. Moreover, there are no further details about that method reported in that study.

In this work, we propose a new global optimization-based multi-region segmentation approach to delineating the whole prostate gland (WG) and its sub-regions: the central gland (CG) and peripheral zone (PZ) simultaneously from the input 3D T2w prostate MR image. The proposed method adapts the prior

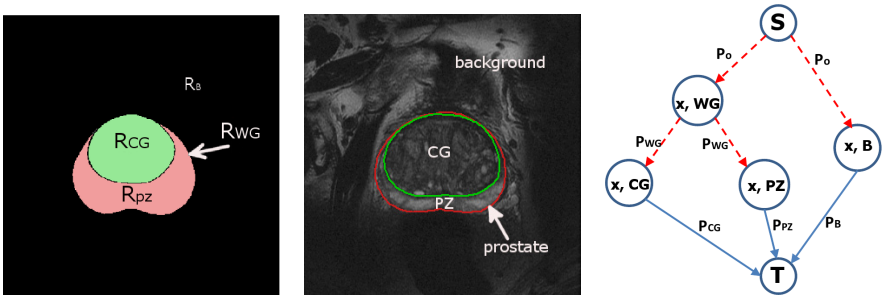

(a) (b) (c)

Fig. 1. Proposed layout of anatomically consistent regions (a) and contours overlaid on a T2w prostate MRI slice (b). The prostate region $\mathcal{R}_B$ is divided into two sub-regions: central gland $\mathcal{R}_{CG}$ and peripheral zone $\mathcal{R}_{PZ}$ and is mutually distinct from the background R_B. (c) shows the proposed spatially continuous flow-maximization scheme.

knowledge of the spatial region consistency to the segmentation of the three prostate-associate regions. We solve the introduced challenging combinatorial optimization problem by means of convex relaxation, for which we propose a novel spatially continuous flow-maximization model and demonstrate its duality to the studied convex relaxed optimization problem with the region consistency constraint. The proposed *continuous max-flow model* directly leads to a new and efficient *continuous max-flow based* algorithm, which enjoys great advantages in numerics and can be readily implemented on GPUs. Experiments over 15 T2-weighted 3D prostate MRIs, by inter- and intra-operator variability, demonstrate the promising performance of the proposed approach.

To our best knowledge, this paper reports the first study on simultaneously extracting the three clinically meaningful regions of prostate: WG, CG and PZ, from 3D T2w MRIs. A similar continuous max-flow based method [16] was proposed in parallel to address the segmentation of cardiac scar tissues from a single Late-Enhancement Cardiac MR Image.

2 Method

We aim to segment a given 3D T2w prostate MR image $I(x)$ into the prostate region $\mathcal{R}_{WG}$ and its two mutually distinct sub-regions: the central gland $\mathcal{R}_{CG}$ and the peripheral zone $\mathcal{R}_{PZ}$, where $\mathcal{R}_B$ denotes the background (see Figure 1(a)), i.e.

$$\Omega \,=\, \mathcal{R}_{WG} \cup \mathcal{R}_B\,, \quad \mathcal{R}_{WG} \cap \mathcal{R}_B \,=\, \emptyset\,, \tag{1}$$

where the two spatially coherent sub-regions: the R_{CG} and R_{PZ} constitute the whole prostate region $\mathcal{R}_{WG}$ such that

$$\mathcal{R}_{WG} \,=\, \mathcal{R}_{CG} \cup \mathcal{R}_{PZ}\,; \quad \mathcal{R}_{CG} \cap \mathcal{R}_{PZ} \,=\, \emptyset\,. \tag{2}$$

The typical T2w prostate MR image shows that each of the zones R_{CG} and R_{PZ} of $\mathcal{R}_{WG}$ has a distinct intensity appearance, hence constituting the complex/inhomogeneous appearance model of the prostate region $\mathcal{R}_{WG}$. This fact makes it challenging to directly extract the correct boundaries of $\mathcal{R}_{WG}$ from the given MRI without taking such region-associated inhomogeneity into account.

We introduce a new multi-region segmentation approach to accurately and efficiently extract $\mathcal{R}_{WG}$ and its sub-regions $\mathcal{R}_{CG}$ and $\mathcal{R}_{PZ}$ simultaneously from the input T2w MR volume, which encodes the complex intensity appearance of prostate by its two visually independent sub-regions and integrate such region consistency prior into the associate optimization problem. In particular, we solve the introduced combinatorial optimization problem by means of convex relaxation, for which we propose a new continuous max-flow model and demonstrate its duality to the investigated convex relaxation problem. The introduced continuous max-flow model directly derives a new multiplier-based algorithm, which enjoys great numerical advantages in simplicity and efficiency.

2.1 Multi-region Segmentation Model and Convex Relaxation

Given the volume image $I(x)$, let $\pi_i(I(x))$, $i \in L(:= \{CG, PZ, B\})$, be the intensity probability density function (PDF) of the respective region $\mathcal{R}_i$. In practice, such intensity PDF models provide a global descriptor of the objects of interest in statistics, which can be learned from either sampled pixels or given training datasets. The appearance models of the two prostate sub-regions $\mathcal{R}_{CG}$ and $\mathcal{R}_{PZ}$ are distinct from each other and, in combination, represent a proper appearance description of the entire prostate region $\mathcal{R}_{WG}$. [17] showed that such a composite intensity appearance model was more accurate than the often-used mixture appearance model [18] in practice.

We therefore define the cost function $D_i(x)$, where $i \in L$, of labeling each pixel x to be in the prostate sub-region $\mathcal{R}_{CG}$, $\mathcal{R}_{PZ}$ or the background region $\mathcal{R}_B$ by the log-likelihood of the respective PDF, i.e.

$$D_i(x) \;=\; -\log\big(\pi_i(I(x))\big)\,, \quad i \in L\,.$$

Consequently, the total labeling cost of segmenting the input prostate MRI $I(x)$ into multiple regions: $\mathcal{R}_{WG} \cup \mathcal{R}_B := \{\mathcal{R}_{CG} \cup \mathcal{R}_{PZ}\} \cup \mathcal{R}_B$ can be formulated by

$$\sum_{i \in L} \int_{\mathcal{R}_i} D_i(x)\, dx\,.$$

In this work, we propose to partition the given volume image $I(x)$ by achieving the minimum of the total labeling cost and area such that

$$\min_{\mathcal{R}_{WG}, \mathcal{R}_B, \mathcal{R}_{CG}, \mathcal{R}_{PZ}} \quad \sum_{i \in L} \int_{\mathcal{R}_i} D_i(x)\, dx \;+\; \sum_{i \in WG \cup L} \int_{\partial \mathcal{R}_i} ds \tag{3}$$

subject to the constraints of the region layout (1) and (2).

Let $u_i(x) \in \{0,1\}, i \in \{WG, CG, PZ, B\}$, be the indicator or labeling function of the corresponding region $\mathcal{R}_i$, such that

$$u_i(x) := \begin{cases} 1\,, & \text{where } x \text{ is inside } \mathcal{R}_i \\ 0\,, & \text{otherwise} \end{cases}, \quad i \in \{WG, CG, PZ, B\}\,.$$

Then, we can identically rewrite the region constraint (1) as

$$u_{WG}(x) + u_B(x) \;=\; 1\,, \quad \forall x \in \Omega \tag{4}$$

and the constraints (2) of the prostate sub-regions by

$$u_{CG}(x) + u_{PZ}(x) \;=\; u_{WG}(x)\,, \quad \forall x \in \Omega\,. \tag{5}$$

Therefore, the optimization problem (3) can be reformulated in terms of the labeling functions $u_i(x) \in \{0,1\}$, $i \in \{WG, CG, PZ, B\}$, as follows

$$\min_{u(x)\in\{0,1\}} \sum_{i\in L} \langle u_i, D_i\rangle \;+\; \sum_{i\in WG\cup L} \int_\Omega g(x)\,|\nabla u_i(x)|\;dx \tag{6}$$

subject to the labeling constraints (4) and (5), where $g(x) \geq 0$ gives the edge weight function and each weighted total-variation function of (6) measures the weighted area of the corresponding surface $\partial\mathcal{R}_i$, $i \in WG \cup L$.

In this study, we solve the challenging combinatorial optimization problem (6) by its convex relaxation:

$$\min_{u(x)\in[0,1]} \sum_{i\in L} \langle u_i, D_i\rangle \;+\; \sum_{i\in WG\cup L} \int_\Omega g(x)\,|\nabla u_i(x)|\;dx \tag{7}$$

subject to the linear equality constraints (4) and (5). The binary-valued labeling funtion $u_i(x) \in \{0,1\}, i \in WG \cup L$, in (3) is relaxed into the convex-set constraint $u_i(x) \in [0,1]$ in (7). Given the convex energy function of (7) and the linear equality constraints (4) and (5), the complicated combinatorial optimization problem (6) is therefore reduced to its convex optimization version (7).

2.2 Dual Optimization Model

Now we introduce the new continuous max-flow approach to solving the proposed *convex relaxed optimization problem* (7) efficiently, which relies on the following flow configuration (similar as [19,20]), see Fig. 1(c):

– We add two terminals s and t as the source and sink of the flows, the two image copies Ω_{WG} and Ω_B (w.r.t. $\mathcal{R}_{WG}$ and $\mathcal{R}_B$) and the two image copies Ω_{CG} and Ω_{PZ} (w.r.t. the prostate sub-regions $\mathcal{R}_{CG}$ and $\mathcal{R}_{PZ}$).

– We link the source s to the same position x of Ω_{WG} and Ω_B, along which an unconstrained source flow $p_o(x)$ is defined. We link any $x \in \Omega_{WG}$ to the same position x at each of Ω_{CG} and Ω_{PZ}, along which an unconstrained prostate flow $p_{WG}(x)$ is defined. In addition, we link each pixel x of Ω_B and $\Omega_{CG,PZ}$ to the

sink t, along which the respective sink flow $p_i(x)$, $i \in L$, is given.
– Additionally, the spatial flow $q_i(x)$, $i \in WG \cup L$, is specified at any x within the image domain Ω_i.

Based upon the above settings of flows, we propose a novel *continuous max-flow model*, which maximizes the total flow streaming from the source s, i.e.

$$\max_{p,q} \quad \int_{\Omega} p_o(x)\, dx \tag{8}$$

subject to
– *Flow capacity constraints*: the sink flows $p_i(x)$, $i \in L$ suffice:

$$p_i(x) \,\leq\, D_i(x)\,, \quad i \in L\,, \tag{9}$$

and the spatial flows $q_i(x)$, $i \in WG \cup L$ suffice:

$$|q_i(x)| \,\leq\, g(x)\,, \quad i \in WG \cup L\,. \tag{10}$$

– *Flow conservation constraints*: the total flow residue vanishes at each x of the image domain Ω_{WG} or Ω_B, i.e.

$$G_i(x) \,:=\, \big(\operatorname{div} q_i - p_o + p_i\big)(x) \,=\, 0\,, \quad i \in \{WG, B\}\,; \tag{11}$$

and the total flow residue also vanishes at each x of Ω_{CG} or Ω_{PZ}, i.e.

$$G_i(x) \,:=\, \big(\operatorname{div} q_i - p_{WG} + p_i\big)(x) \,=\, 0\,, \quad i \in \{CG, PZ\}\,. \tag{12}$$

Now we introduce the multiplier functions $u_i(x)$ to the flow conservation constraints of (11) and (12) in the *continuous max-flow model* (8) , which results in the *primal-dual model* equivalen to (8):

$$\max_{p,q} \min_{u} \;\; L(u; p, q) \,:=\, \int_{\Omega} p_o(x)\, dx \,+\, \sum_{i \in WG \cup L} \langle u_i, G_i \rangle \tag{13}$$

subject to (9) and (10).

Through analysis, we can prove the duality between the introduced three optimization models (8), (13) and (7):

Proposition 1. *The* continuous max-flow model (8)*, the* primal-dual model (13) *and the* convex relaxed optimization model (7) *are dual (equivalent) to each other, i.e.,*

$$(8) \iff (13) \iff (7)\,.$$

Its proof is omitted due to the limited space.

2.3 Duality-Based Algorithm

By Prop. 1, it is easy to see that the *convex relaxed optimization model* (7) can be solved equally by computing the *continuous max-flow model* (8). Moreover, by

the *primal-dual model* (13) which is equivalent to the (8), the labeling functions $u_i(x)$, $i \in WG \cup L$, work as the multipliers to the corresponding linear equalities (11) and (12) of flow conservation, and the energy function of (13) is just the associated Lagrangian function of the *continuous max-flow model* (8). Hence, an efficient *continuous max-flow algorithm* can be derived upon the augmented multiplier algorithmic scheme [21], which iteratively optimizes the associated augmented Lagrangian function:

$$\max_{p,q} \min_{u} L_c(u; p, q) := L(u; p, q) - \frac{c}{2} \sum_{i \in WG \cup L} \|G_i\|^2$$

subject to the flow capacity constraints (9) and (10), where $L(u; p, q)$ is the Lagrangian function (13). Typically, each k-th iteration of the algorithm maximizes the $L_c(u; p, q)$ over the flow functions p and q subject to the flow constraints (9) and (10), and simply updates the labeling functions $u_i(x)$, $i \in WG \cup L$, afterwards (the detailed algorithimic scheme is similar as in [19,20] and omitted here due to the limited space).

3 Experiments and Results

Image Acquisition. We applied the proposed continuous max-flow algorithm on 15 T2w MR images acquired using a body coil. Subjects were scanned at 3 Tesla with a GE Excite HD MRI system (Milwaukee, WI, USA). All images were acquired at $512 \times 512 \times 36$ voxel with spacing of $0.27 \times 0.27 \times 2.2$ mm^3.

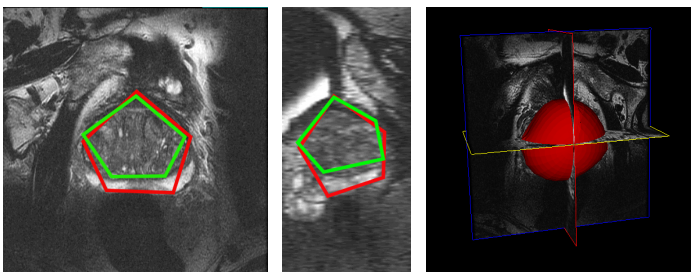

(a) (b) (c)

Fig. 2. Initialization scheme. (a) Axial view, (b) Sagital view, (c) orthogonal view overlapped with an initial WG surface. Initial polygon generated by user-selected points for WG (red), and CG (green).

Initialization. The segmentation is initialized by two closed surfaces, which are used to approximate the CG and WG boundaries, respectively. Each of these surfaces is constructed via a thin-plate spline fitting with the positioning of ten to twelve initial points on the prostate or CG surface: half on the axial view and half of the points on the sagittal view. Figure 2 shows example initializations for

WG and CG surfaces, respectively. The smooth closed surface approximates the prostate shape and provides a reasonably good initialization condition (see [22] for more details). The original input volume image is cropped by enlarging the bounding box of the initial WG surface by 30 voxels in each component direction in order to speed up computations. The initial PDFs for each region R_{WG}, R_B, R_{CZ} and R_{PZ}, are calculated based on the user-initialized surfaces, respectively.

Evaluation Metrics. We evaluated the proposed segmentation method by comparing the algorithm to manual segmentation results using Dice similarity coefficient (DSC), the mean absolute surface distance (MAD) and the maximum absolute surface distance (MAXD) [23,24]. Each prostate image was sub-divided into three regions, base, mid-gland and apex, according to the apex-base axis of the manual segmented prostate surface (respectively 0.3, 0.4, 0.3 of the length of the base-apex axis) [25]. All validation metrics were calculated for the entire prostate gland, central gland and peripheral zone in the three respective regions. In addition, the coefficient-of-variation (CV) [26] of DSC was used to evaluate the intra- and inter-observer variability of our method.

Accuracy. Table. 1 shows the segmentation result for 15 patient images using the proposed method. In average the DSC was $89.1 \pm 3.3\%$ for the whole prostate gland, $82.3 \pm 2.9\%$ for the central gland, and $69.3 \pm 6.8\%$ for the peripheral zone. More specifically, our method is capable of generating good segmentation accuracy for the base-, mid- and apex-section of CG and WG. DSCs for the base-

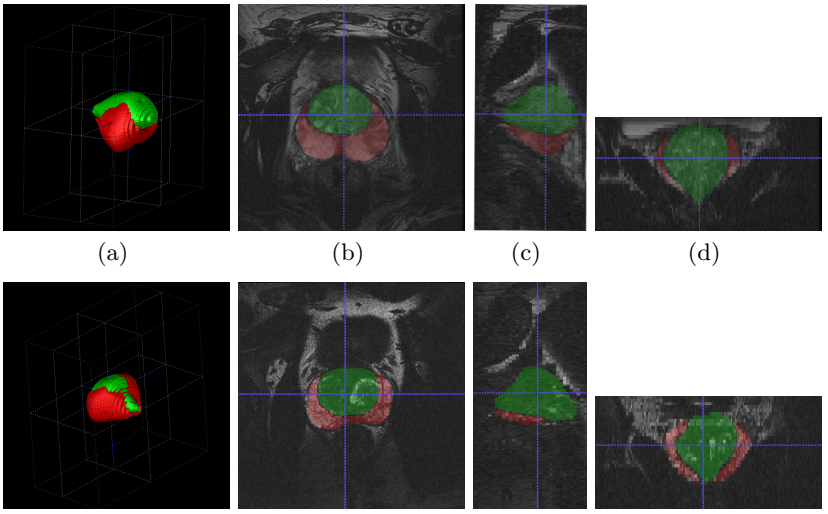

Fig. 3. Segmentation result of two prostates. Column 1 to column 4: resulting surface, axial view, sagittal view, and coronal view, respectively. Red: the segmented PZ, green: the segmented CG.

Table 1. Overall segmentation accuracy for 15 patient images

	DSC (%)			
	total	base	mid	apex
PZ	69.3 ± 6.8	54.7 ± 20.8	81.8 ± 5.0	60.1 ± 12.2
CG	82.3 ± 2.9	81.1 ± 2.9	92.0 ± 2.5	68.0 ± 8.1
WG	89.1 ± 3.3	84.5 ± 3.3	94.5 ± 1.6	87.2 ± 5.0
	MAD (voxels)			
	total	base	mid	apex
PZ	2.5 ± 0.8	4.4 ± 3.0	2.0 ± 0.7	2.2 ± 1.6
CG	2.9 ± 1.0	3.3 ± 1.5	3.5 ± 2.2	3.7 ± 1.4
WG	1.7 ± 0.5	2.6 ± 1.6	2.2 ± 0.9	1.8 ± 0.7
	MAXD (voxels)			
	total	base	mid	apex
PZ	20.8 ± 14.0	35.4 ± 24.6	15.0 ± 12.6	15.2 ± 9.6
CG	15.0 ± 15.5	17.0 ± 16.0	15.3 ± 15	19.6 ± 9.9
WG	7.9 ± 3.9	13.8 ± 10.4	10.8 ± 4.3	17.9 ± 6.9

and apex-PZ are comparably low and have large standard deviation ($54.7 \pm 20.8\%$ and $60.1 \pm 12.2\%$, respectively) since the segmentation for these two regions is more challenging even for radiologists using manual segmentation due to the low degree of recognition of such a thin structure interfered by partial volume effects and unclear boundaries between the zones. However, a DSC of $81.8 \pm 5.0\%$ for mid-PZ is favourable, which could meet clinical requirements. In addition, the evaluation results of MAD and MAXD are provided in Table. 1, which provides similar consistent information to DSC.

Reproducibility. Ten images were randomly selected for evaluating the reproducibility of the proposed method. The entire PZ, CG, and WG for each prostate were taken into account instead of their separate sections (apex, mid and base). Each image was segmented five times by the same observer for assessing intra-observer variability in terms of DSC. Figure 4(a) depicts the results for the intra-observer variability. A mean coefficient-of-variation (CV) of 9.25%, 1.63%, and 3.36% was found for PZ, CG, and WG, respectively. To evaluate the variability introduced by manual initialization, ten images were also segmented by other three blinded users. The proposed method initialized by the three users yielded a mean CV of 9.43%, 1.71%, and 3.47% for PZ, CG, and WG, respectively (Fig. 4(b)). It can be seen that the proposed method has low variability of both intra- and inter-observer segmentation for CG and WG, but the observer variability is higher for PZ.

Computation Time. The proposed *continuous max-flow algorithm* was implemented on GPUs (CUDA, NVIDIA Corp., Santa Clara, CA) and the user

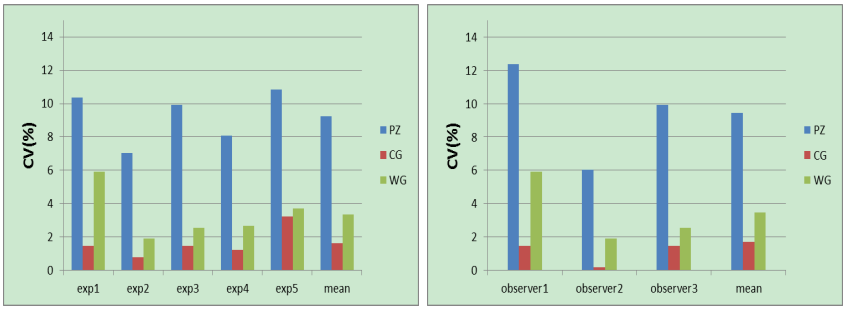

(a) intra-observer variability (b) inter-observer variability

Fig. 4. Result of intra- and inter-observer variabilities in terms of the coefficient-of-variation (CV) of DSC

interface in Matlab (Natick, MA). The experiments were conducted on a Windows desktop with an Intel i7-2600 CPU (3.4 GHz) and a GPU of NVIDIA Geforce 580X. The segmentation time was calculated as the mean run time of five repeated segmentations for each 3D MR image: for each patient image, the proposed algorithm took 5 ± 0.5s in addition to 35 ± 5s for initialization, and resulted in less than 1 minute in total to segment one image volume.

4 Discussion and Conclusion

In this work, we propose and evaluate a new convex optimization-based multi-region segmentation approach to simultaneously extracting the boundaries of prostate and its component zones from the input 3D prostate T2w MRI, which addresses the challenge of segmenting multiple prostate regions in a numerically sound and efficient manner. The introduced algorithm shows reliable performance results with minimal user interactions using 15 patient images and suggests itself for use in 3D TRUS/MR image guided prostate interventions and computer aided diagnosis of prostate cancer.

The experiments showed that the proposed approach was capable of jointly segmenting different prostate zones with promising accuracy, intra- and inter-observer variability. In terms of accuracy, DSCs of $69.3 \pm 6.8\%$ and $82.3 \pm 2.9\%$ for PZ and CG yielded by our methods were lower than $75.0 \pm 7.0\%$ and $89.0 \pm 3.0\%$ reported in [15] or $76.0 \pm 6.0\%$ and $87.0 \pm 4.0\%$ reported in [14]. However, both methods of [15,14] made use of multi-spectral MR information and relied on the manual segmentation of WG as initialization. Moreover, comparing to those methods, the proposed method required fewer user interactions in practice.

On the other hand, the proposed method can provide good segmentation accuracy for PZ, CG, and WG in the mid-prostate section, which is highly desirable during image-guided prostate interventions and cancer diagnosis. To further improve the segmentation accuracy in the basal and apical regions, future

studies will focus on incorporating additional prior knowledge, such as texture, shapes or information from multi-spectral MR imaging.

Acknowledgments. The authors are grateful for the funding support from the Canadian Institutes of Health Research (CIHR), the Ontario Institute of Cancer Research (OICR), and the Canada Research Chairs (CRC) Program for this work.

References

1. Siegel, R., Naishadham, D., Jemal, A.: Cancer statistics, 2012. CA: A Cancer Journal for Clinicians 62(1), 10–29 (2012)
2. Leslie, S., Goh, A., Lewandowski, P.M., Huang, E.Y.H., de Castro Abreu, A.L., Berger, A.K., Ahmadi, H., Jayaratna, I., Shoji, S., Gill, I.S., Ukimura, O.: 2050 contemporary image-guided targeted prostate biopsy better characterizes cancer volume, gleason grade and its 3d location compared to systematic biopsy. The Journal of Urology 187(4, suppl.), e827 (2012)
3. Doyle, S., Feldman, M.D., Tomaszewski, J., Madabhushi, A.: A boosted bayesian multiresolution classifier for prostate cancer detection from digitized needle biopsies. IEEE Trans. Biomed. Engineering 59(5), 1205–1218 (2012)
4. Beyersdorff, D., Winkel, A., Hamm, B., Lenk, S., Loening, S.A., Taupitz, M.: MR imaging-guided prostate biopsy with a closed MR unit at 1.5 T: initial results. Radiology 234(2), 576–581 (2005)
5. McNeal, J.E.: The zonal anatomy of the prostate. The Prostate 2(1), 35–49 (1981)
6. Villeirs, G., De Meerleer, G.: Magnetic resonance imaging (mri) anatomy of the prostate and application of mri in radiotherapy planning. European Journal of Radiology 63(3), 361–368 (2007)
7. Haffner, J., Potiron, E., Bouyé, S., Puech, P., Leroy, X., Lemaitre, L., Villers, A.: Peripheral zone prostate cancers: location and intraprostatic patterns of spread at histopathology. The Prostate 69(3), 276–282 (2009)
8. Reinsberg, S., Payne, G., Riches, S., Ashley, S., Brewster, J., Morgan, V., et al.: Combined use of diffusion-weighted mri and 1h mr spectroscopy to increase accuracy in prostate cancer detection. American Journal of Roentgenology 188(1), 91–98 (2007)
9. Kitajima, K., Kaji, Y., Fukabori, Y., Yoshida, K., Suganuma, N., Sugimura, K.: Prostate cancer detection with 3 t mri: Comparison of diffusion-weighted imaging and dynamic contrast-enhanced mri in combination with t2-weighted imaging. Journal of Magnetic Resonance Imaging 31(3), 625–631 (2010)
10. Kirby, R., Gilling, P.: Fast facts: benign prostatic hyperplasia. Health Press Limited (2011)
11. Ghose, S., Oliver, A., Martí, R., Lladó, X., Vilanova, J., Freixenet, J., Mitra, J., Sidibé, D., Meriaudeau, F.: A survey of prostate segmentation methodologies in ultrasound, magnetic resonance and computed tomography images. Computer Methods and Programs in Biomedicine 108(1), 262–287 (2012)
12. Allen, P., Graham, J., Williamson, D., Hutchinson, C.: Differential segmentation of the prostate in mr images using combined 3d shape modelling and voxel classification. In: 3rd IEEE International Symposium on Biomedical Imaging: Nano to Macro, pp. 410–413. IEEE (2006)

13. Yin, Y., Fotin, S., Periaswamy, S., Kunz, J., Haldankar, H., Muradyan, N., Turkbey, B., Choyke, P.: Fully automated 3d prostate central gland segmentation in mr images: a logismos based approach. In: SPIE, p. 83143B (2012)
14. Makni, N., Iancu, A., Colot, O., Puech, P., Mordon, S., Betrouni, N., et al.: Zonal segmentation of prostate using multispectral magnetic resonance images. Medical Physics 38(11), 6093 (2011)
15. Litjens, G., Debats, O., van de Ven, W., Karssemeijer, N., Huisman, H.: A pattern recognition approach to zonal segmentation of the prostate on MRI. In: Ayache, N., Delingette, H., Golland, P., Mori, K. (eds.) MICCAI 2012, Part II. LNCS, vol. 7511, pp. 413–420. Springer, Heidelberg (2012)
16. Rajchl, M., Yuan, J., White, J.A., Nambakhsh, C.M.S., Ukwatta, E., Li, F., Stirrat, J., Peters, T.M.: A fast convex optimization approach to segmenting 3D scar tissue from delayed-enhancement cardiac MR images. In: Ayache, N., Delingette, H., Golland, P., Mori, K. (eds.) MICCAI 2012, Part I. LNCS, vol. 7510, pp. 659–666. Springer, Heidelberg (2012)
17. Delong, A., Gorelick, L., Schmidt, F.R., Veksler, O., Boykov, Y.: Interactive segmentation with super-labels. In: Boykov, Y., Kahl, F., Lempitsky, V., Schmidt, F.R. (eds.) EMMCVPR 2011. LNCS, vol. 6819, pp. 147–162. Springer, Heidelberg (2011)
18. Yuan, J., Qiu, W., Ukwatta, E., Rajchl, M., Sun, Y., Fenster, A.: An efficient convex optimization approach to 3D prostate MRI segmentation with generic star shape prior. In: Prostate MR Image Segmentation Challenge, MICCAI (2012)
19. Yuan, J., Bae, E., Tai, X.-C., Boykov, Y.: A continuous max-flow approach to potts model. In: Daniilidis, K., Maragos, P., Paragios, N. (eds.) ECCV 2010, Part VI. LNCS, vol. 6316, pp. 379–392. Springer, Heidelberg (2010)
20. Yuan, J., Bae, E., Tai, X.: A study on continuous max-flow and min-cut approaches. In: CVPR 2010 (2010)
21. Bertsekas, D.P.: Nonlinear Programming. Athena Scientific (September 1999)
22. Hu, N., Downey, D.B., Fenster, A., Ladak, H.M.: Prostate boundary segmentation from 3D ultrasound images. Med. Phys. 30(7), 1648–1659 (2003)
23. Qiu, W., Yuan, J., Ukwatta, E., Tessier, D., Fenster, A.: Rotational-slice-based prostate segmentation using level set with shape constraint for 3D end-firing TRUS guided biopsy. In: Ayache, N., Delingette, H., Golland, P., Mori, K. (eds.) MICCAI 2012, Part I. LNCS, vol. 7510, pp. 537–544. Springer, Heidelberg (2012)
24. Qiu, W., Yuan, J., Ukwatta, E., Tessier, D., Fenster, A.: Prostate segmentation in 3d TURS using convex optimization with shape constraint. In: SPIE, Medical Imaging (2013)
25. Mahdavi, S.S., Moradi, M., Wen, X., Morris, W.J., Salcudean, S.E.: Evaluation of visualization of the prostate gland in vibro-elastography images. Medical Image Analysis 15(4), 589–600 (2011)
26. Zou, K.H., McDermott, M.P.: Higher-moment approaches to approximate interval estimation for a certain intraclass correlation coefficient. Statistics in Medicine 18(15), 2051–2061 (1999)